NASA Technical Memorandum 102758

HOT-BENCH SIMULATION OF THE ACTIVE FLEXIBLE WING WIND-TUNNEL MODEL

CAREY S. BUTTRILL
JACOB A. HOUCK

NOVEMBER 1990

(NASA-TM-102758) HOT-BENCH SIMULATION OF THE ACTIVE FLEXIBLE WING WIND-TUNNEL MODEL (NASA) 14 p CSCL 01C

N91-21144

Unclas
G3/08 0330164

National Aeronautics and Space Administration

Langley Research Center
Hampton, Virginia 23665

HOT-BENCH SIMULATION OF THE ACTIVE FLEXIBLE WING WIND-TUNNEL MODEL

Carey S. Buttrill* and Jacob A. Houck**
NASA Langley Research Center
Hampton, Virginia 23665-5225

Abstract

Two simulations, one batch and one real-time, of an aeroelastically scaled wind-tunnel model were developed. The wind-tunnel model was a full-span, free-to-roll model of an advanced fighter concept. The batch simulation was used to generate and verify the real-time simulation and to test candidate control laws prior to implementation. The real-time simulation supported hot-bench testing of a digital controller, which was developed to actively control the elastic deformation of the wind-tunnel model. Time scaling was required for hot-bench testing. The wind-tunnel model, the math models for the simulations, the techniques employed to reduce the hot-bench time-scale factor, and the verification procedures are described.

Nomenclature

a_δ first-order pole of typical actuator transfer function, rad/sec

$[A_k^{ff}]$ $n_f x n_f$ matrix where $A_0^{ff}(i,j) = \dfrac{\partial(-F^{\eta i}/\bar{q})}{\partial \eta_j^{(k)}}$, negative force coefficient on the i^{th} elastic mode due to k^{th} time derivative of j^{th} elastic mode, k = 0,1,2

$[A_{m+2}^{ff}]$ $n_f x n_f$ matrix where $A_{m+2}^{ff}(i,j) = \dfrac{\partial(-\dot{x}_{im}^f)}{\partial \dot{\eta}_j}$, effect of j^{th} elastic mode rate on the derivative of the m^{th} unsteady aerodynamic lag state associated with the i^{th} flexible mode, $m = 1,...,n_{lag}$

$[A_k^{fc}]$ $A_k^{fc}(i,j) = \dfrac{\partial(-F^{\eta i}/\bar{q})}{\partial \delta_j^{(k)}}$, force on i^{th} elastic mode due to k^{th} time derivative of j^{th} control mode, k = 0,1,2

$[A_k^{cf}]$ $A_k^{fc}(i,j) = \dfrac{\partial(-F^{\delta i}/\bar{q})}{\partial \eta_j^{(k)}}$, opposing hinge moment on i^{th} control mode due to k^{th} time derivative of j^{th} elastic mode

[A],[B] general continuous system dynamic matrices
[C],[D]

$\bar{c}$ wing chord, 39.76 in

$F^{\eta i}$ total generalized force on elastic (flexible) mode i

[F],[G] general discrete system dynamic matrices

$[G_0]$ discrete system input matrix applied to $\{u_k\}$

$[G_1]$ discrete system input matrix applied to $\{u_{k+1}\}$

$[G^f]$ diagonal modal damping matrix, $G^f(i,i) = .03$

h integration step size, seconds

HM_δ control surface hinge moment, in-lbs

k_δ actuator steady state gain

$[K^f]$ diagonal modal stiffness matrix, $K^f(i,i) = m_i\omega_i^2$

$[M^f]$ diagonal modal mass matrix, $M^f(i,i) = m_i$

$[M^{cf}]$ matrix of control mode to elastic mode inertial coupling

$\bar{q}$ dynamic pressure, lbs/in^2

rl rate limit

s Laplace variable

$\{u_k\}$ vector input at time t=kh

V airspeed, in/sec (6696 in/sec at Mach = .5)

x state

$\{x_k\}$ state vector at time t=kh

δ_i generalized coordinate - control mode i

ζ_δ damping of second-order denominator term of typical actuator transfer function, rad/sec

η_i generalized coordinate - elastic mode i

ξ_g output of Dryden turbulence transfer function

ρ density, $1.146x10^{-7}$ lbs-sec^2/in^4 or slinches/in^3

σ_g RMS turbulence intensity, in/sec

υ Gaussian random number

ω_δ frequency of second-order denominator term of typical actuator transfer function, rad/sec

ω_g break frequency of turbulence transfer function, $(2\pi)(17.32)$ rad/sec

ω_{aa} break frequency of anti-aliasing transfer function, $(2\pi)(25.0)$ rad/sec

[] matrix

{} column vector

Subscripts

a aerodynamic
aa anti-aliasing
as anti-symmetric
c commanded
g quantity associated with turbulence
lag aerodynamic "lag" quantity
lin linear
neg negative
pos positive
nl no load
STALL actuator dynamic stall value
sy symmetric
0 quantity associated with position
1 quantity associated with rate
2 quantity associated with acceleration
δ quantity associated with actuator

* Senior Member, AIAA
** Associate Fellow, AIAA

Superscripts

f	associated with elastic (flex) mode equations
ff	effect on elastic due to elastic (flex-flex)
fc	effect on elastic due to control (flex-control)
fg	effect on elastic due to gust input (flex-gust)
c	associated with control mode equations
cf	effect on hinge moment due to flex (control-flex)
cc	effect on hinge moment due to control
cg	effect on hinge moment due to gust input

Abbreviations

AB2	Adams-Bashforth second-order predictor
AFW	Active Flexible Wing
CAMAC	Computer Automated Measurement and Control
ISAC	Interaction of Structures, Aerodynamics, and Controls
LaRC	Langley Research Center
LEI	Leading Edge Inboard
LEO	Leading Edge Outboard
PPU	Peripheral Processor Unit
psf	pounds per square foot
RK2	Runge-Kutta second-order predictor-corrector
RMS	root-mean-square
RVDT	Rotary Variable Differential Transducer
TDT	LaRC Transonic Dynamics Tunnel
TEI	Trailing Edge Inboard
TEO	Trailing Edge Outboard

Introduction

The simulations described in this paper were developed as part of the ongoing Active Flexible Wing Wind-Tunnel Test Program,[1,2,3] a collaborative effort between NASA Langley Research Center and Rockwell International Corporation. Three wind-tunnel tests have been completed and the final test is scheduled for February 1991. The program objective is the validation of analysis and synthesis methodologies as applied to the multi-function control of a sophisticated aeroelastic wind-tunnel model. The control functions being investigated include suppression of flutter, roll performance maximization, and load alleviation. Only the simulation models developed to support flutter suppression are discussed in this paper. Flutter is a potentially explosive dynamic instability that can occur when a sufficiently flexible wing begins to extract energy from the fluid stream. During the most recent tunnel entry, completed in November 1989, flutter suppression was successfully demonstrated at a dynamic pressure 24 percent above a measured open-loop flutter point.[2,3]

Simulation Roles

Two distinct, but interrelated, simulations were developed to support the AFW test program, a batch simulation and a real-time simulation. The batch simulation served as a "truth" model, and was used to: (1) evaluate the control laws to predict performance and establish gain and phase margins; (2) provide models and data files for the real-time hot-bench simulation; and (3) verify the real-time simulation.

The real-time simulation of the model/wind-tunnel environment served to verify the functionality of the digital controller system in a hot-bench laboratory. End-to-end verification and debugging of the complex, one-of-a-kind digital controller system was essential, since whenever flutter testing is undertaken, both the model and the tunnel are at risk.

Wind-Tunnel Model

Figure 1 shows the AFW model mounted in the LaRC Transonic Dynamics Tunnel during the November 1989 test. The sting mount has an internal ball bearing arrangement that allows the model to roll +/- 145° about the sting axis. The fuselage is connected to the sting with a hydraulically powered pivot so that the model can be remotely pitched from approximately -1.5° to +13.5°. Destabilizing mass ballast was added to each wingtip so that the model would flutter within the operating envelope of the TDT[2]. The tip ballast serves to lower both the first-bending and the first-torsion elastic mode frequencies, with the predominant effect on the first-torsion mode. The result is that the first-torsion and the first-bending elastic modes combine to form the primary flutter mechanism at a lower dynamic pressure than was the case for the original model (with no tip ballast). The tip ballast can also be rapidly decoupled in pitch from the wingtip by releasing a hydraulic brake. When decoupled, the tip ballast is restrained in pitch by a soft spring. Decoupling the tip ballast proved to be an effective flutter stopper during testing, providing a significant safety margin. For the flutter

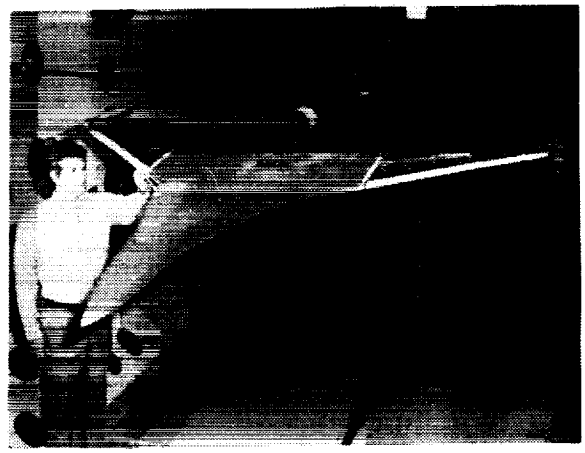

Figure 1.- AFW model mounted in the LaRC Transonic Dynamics Tunnel.

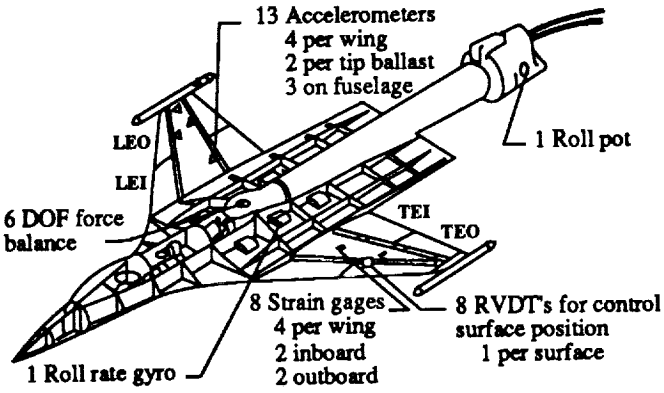

Figure 2.- Instrumentation of the AFW model.

suppression tests conducted in the November 1989 test, the roll brake was engaged, so that the model was not free to roll.

Figure 2, a drawing of the model, illustrates the locations of the control surfaces and selected instrumentation. There are 8 control surfaces and 13 accelerometers. With the addition of the tip ballast, two wing accelerometers, previously co-located with the leading edge inboard control surfaces, were moved to the tip ballasts. Reference 4 describes in detail the AFW wind-tunnel model prior to adding the tip ballast. The input/output signal list for both the wind-tunnel model and the supporting simulations is given in Appendix A.

Hot-Bench Laboratory

The AFW hot-bench simulation set-up, depicted schematically in figure 3, utilized the central real-time facility at LaRC[5]. The LaRC real-time facility consists of nodes or simulation sites that communicate by means of a 50-megabit-per-second fiber-optic digital-data network. The various simulation nodes on the network included two Control Data Cyber 175 computers, engineering control consoles, various aircraft cockpits, and motion base hardware. For the AFW hot-bench simulation, one Cyber 175 was used to integrate the equations of motion. An Adage graphics computer, used in this study, communicates directly with a Cyber 175 through a port. New Terabit Eagle 1000 graphics computers, currently being installed at LaRC, will communicate over the fiber-optic network as another simulation node. Communications with the digital controller occurred over analog lines in the same manner as when the controller was connected to the wind-tunnel model at the LaRC TDT.

Real-Time Graphics

To assist in visualizing the simulated model dynamic behavior, a real-time display (figure 4) was developed on an ADAGE graphics computer. The display presents model pitch and roll, control surface deflections, and total structural deformation of the simulated wind-tunnel model. The display is based on a finite-element structural model of the test article. A subset of the finite-element structural nodes were used to highlight the main body, wings, and the eight control surfaces. The dashed line represents the undeformed configuration. The deformations can be exaggerated for ease of viewing by a factor set at the console.

Simulation Time Scaling

The AFW hot-bench simulation operated at a time scale slower than 1:1 (real time). Time-scale is a function of the integration step (h) and the computer frame (T). If T is larger than h, the simulation runs at 1:(T/h) "slow." Since there was no human operator in the hot-bench loop, a time scale other than 1:1 could be accommodated. Several factors prevented the AFW hot-bench simulation from operating in real time. The control computer was scheduled to run at 200 Hz in the wind-tunnel. To avoid excessive digitally induced time delays, the hot-bench simulation needed to update at least twice for each digital controller frame, requiring a 400 Hz rate for the simulation if it were to run in real time. The minimum frame time available on the Cyber 175 real-time clock was 5 milliseconds (200 Hz). The simulation model itself was sufficiently complex that a computational frame of at least 12.5 milliseconds (80 Hz) was required. Furthermore, since there are only two Cyber real-time computers and many real-time jobs, the hot-bench simulation often shared a Cyber 175 with another job. With only one half of the Cyber computing power available, the 80 Hz simulation update rate would be further reduced to 40 Hz. Time-scale must, therefore, be an easily adjusted parameter for any dynamic component in the hot-bench loop.

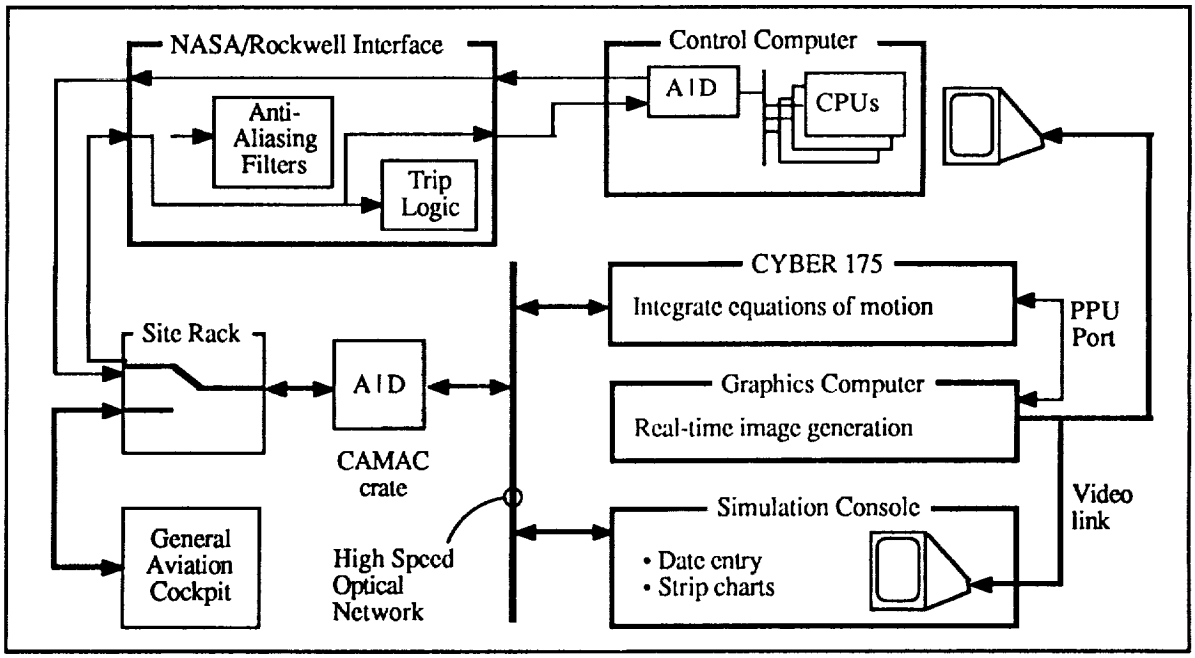

Figure 3.- Schematic of the AFW hot-bench simulation laboratory.

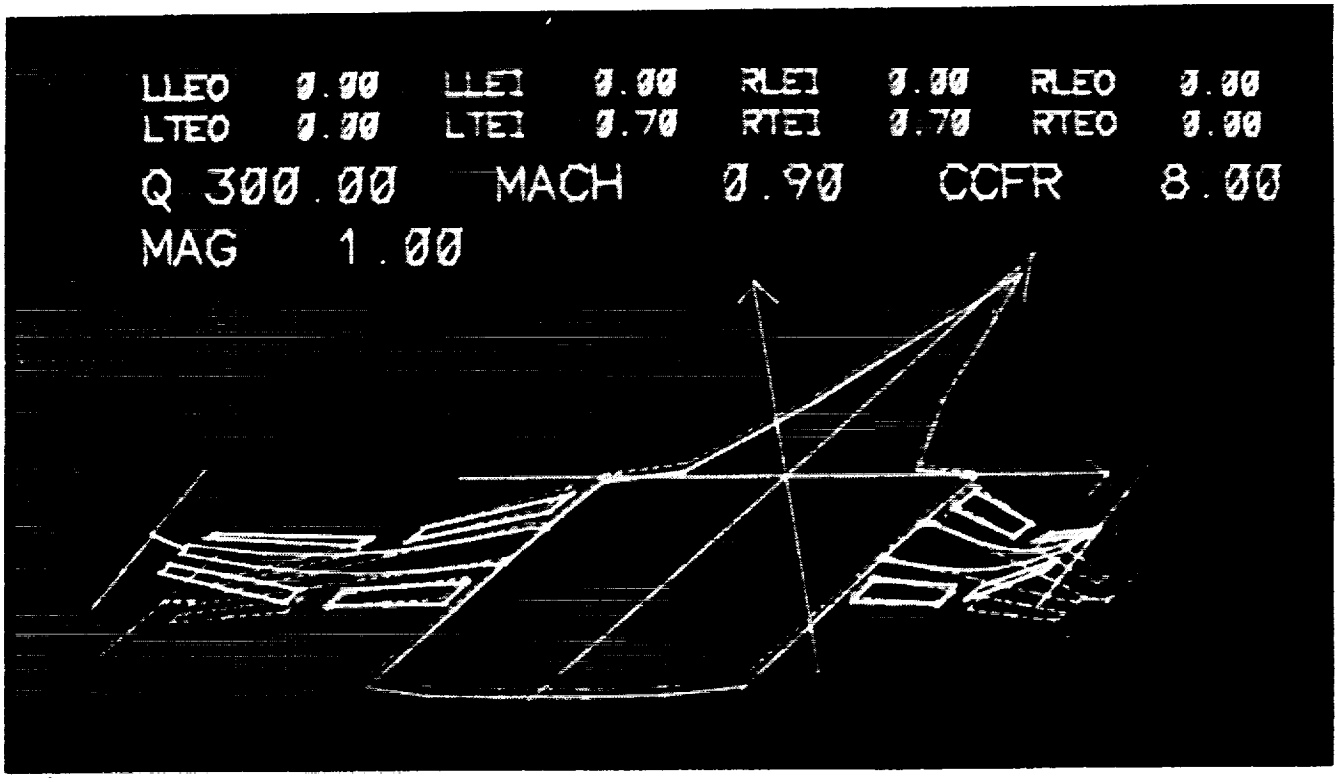

Figure 4.- Adage generated real-time wireframe image of the simulated AFW model.

Digital Controller Apparatus

The control computer consisted of a SUN 3/160 workstation augmented with a digital signal processor, a floating point array processor, and analog/digital conversion boards.[2,6] During both hot-bench and tunnel testing, signals to and from the digital controller go through a Rockwell-NASA interface box. The interface box has several functions, one of which is to house anti-aliasing filters that condition the signals from the wind-tunnel model before being sampled by the digital controller. Because of the time scaling, the anti-aliasing filters in the interface box were bypassed during hot-bench testing (figure 1). The anti-aliasing filter dynamics were included in the hot-bench simulation. Since the control laws were digitized assuming an update rate of 200 Hz in the wind tunnel, when the hot-bench simulation ran at 1:n slow, the controller was clocked at (200/n) Hz to be dynamically equivalent.

In addition to its primary function of implementing a selected control law at 200 Hz, the digital controller performed a variety of support functions. Static checks, dynamic data acquisition and storage, and sine-sweeps were performed. Data from 20 second sine-sweeps were shipped to another computer wherein both open-loop and closed-loop plant estimations were performed.[7]

Simulation Math Model

Linear aeroelastic descriptions for the symmetric and anti-symmetric boundary conditions were generated using a set of aeroservoelastic design and analysis programs developed at the LaRC called ISAC, short for "Interaction of Structures, Aerodynamics, and Controls"[8]. Doublet lattice aerodynamic theory was used. These models were combined with empirical data to form a "whole aircraft" model wherein left and right actuators were modeled individually.

Actuators

Frequency responses for the eight individual actuators were measured with the wing elastic motion restrained. In the frequency range of interest, third-order transfer functions, with parameters optimized in a least square sense, produced good fits with measured frequency response data. In general, right and left members of an actuator pair required different parameters to achieve a good fit and were so modeled.

All the actuator transfer functions had the following form,

$$\frac{\delta(s)}{\delta_c(s)} = \frac{k_\delta\, a_\delta\, \omega_\delta^2}{(s+a_\delta)(s^2 + 2\zeta_\delta\omega_\delta s + \omega_\delta^2)}$$

where k_δ is the steady state gain, a_δ is the first-order pole location, ζ_δ is the damping of the complex pair, and ω_δ is the frequency of the complex pair. The second-order complex pair results from the compressibility of the hydraulic fluid together with compliance of the structure. The first-order pole reflects the dynamics of hydraulic fluid flowing through a small orifice whose size is regulated by position feedback error. Rate limits, as a function of load, were specified by the manufacturer and result from the maximum rate that hydraulic fluid can pass through a small orifice for a given difference between supply and chamber pressures. The first-order pole part of the transfer function was then a reasonable place to apply rate limits. An initial, linear rate was first calculated as

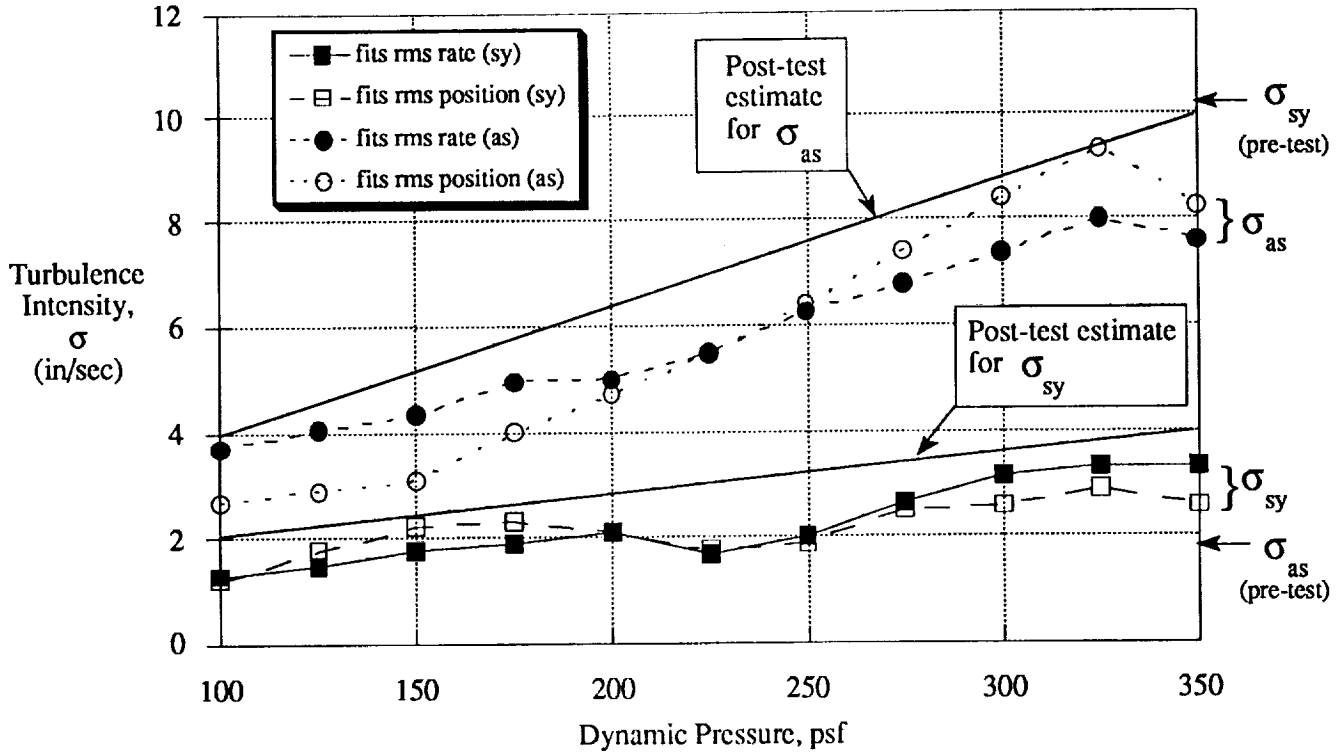

Figure 5.- Turbulence intensities used for simulation.

follows,

$$\dot{x}_{0_{lin}} = k_\delta a_p (\delta_c - x_0)$$

Positive and negative rate limits based on no-load rate limits modified by hinge moment were formed,

$$rl_{pos} = (rl_{nl})\sqrt{1-(HM_\delta/HM_{\delta_{STALL}})}$$

$$rl_{neg} = -(rl_{nl})\sqrt{1+(HM_\delta/HM_{\delta_{STALL}})}$$

where the hinge moment, HM_δ, is positive for an external load resisting positive actuator motion, and $HM_{\delta_{STALL}}$ represents the maximum load the actuators can overcome. Note that an aiding load will produce a rate limit larger than the no-load rate limit, rl_{nl}. An aiding load could occur for a leading edge surface. The positive and negative limits were imposed on the linear rate $\dot{x}_{0_{lin}}$ as follows,

$$\dot{x}_0 = \begin{cases} rl_{pos} & \text{if } \dot{x}_{0_{lin}} > rl_{pos} \\ \dot{x}_{0_{lin}} & \text{otherwise} \\ rl_{neg} & \text{if } \dot{x}_{0_{lin}} < rl_{neg} \end{cases}$$

The state x_0 was then used as a command to the second-order portion of the actuator transfer function

$$\ddot{\delta} = \omega_\delta^2 (x_0 - \delta) - 2\zeta_\delta \omega_\delta \dot{\delta}$$

Once the position, velocity, and acceleration of the control surfaces were obtained they were resolved into symmetric and anti-symmetric components that became inputs into the aeroelastic equations.

Turbulence Model

A turbulence model based on the Dryden atmospheric turbulence model[9] was used. A break frequency of 17.23 Hz for the turbulence transfer function was used to approximate the expected wind-tunnel turbulence. Resonance peaks at 10 Hz were observed in tunnel data from prior entries and 10-11 Hz was the predicted flutter frequency. A break frequency of 17.23 Hz produces a peak magnitude at 10 Hz in the Dryden transfer function. The state equations used for each symmetry are,

$$\ddot{x}_g = -2\omega_g \dot{x}_g - \omega_g^2 x_g + \sigma_g \omega_g^{3/2} T_\upsilon^{1/2} \upsilon$$

where, υ is a Gaussian random process that is sampled and held every T_υ seconds, ω_g is the break frequency in radians/second, and σ_g is the RMS intensity. In both the batch and hot-bench simulations, T_υ is the integration step size. The factor of $T_\upsilon^{1/2}$ applied to the input υ arises from the inherently band-limited nature of a digital simulation. The random process that produces υ can be interpreted as white noise being passed through a perfect $(1/2T_\upsilon)$ Hz band-pass filter. The output equations are,

$$\xi_g = x_g + \frac{\sqrt{3}}{\omega_g}\dot{x}_g \quad \text{and} \quad \dot{\xi}_g = \dot{x}_g + \frac{\sqrt{3}}{\omega_g}\ddot{x}_g$$

Prior to the November 1989 entry, an overall intensity level of 12 in/sec was estimated for the tunnel turbulence. It was decided to allocate the turbulence between the symmetric and anti-symmetric models based on an 85/15 percent distribution. The following symmetric and anti-symmetric intensities resulted

$$\sigma_{g_{sy}} = 10.2 \text{ in/sec} \quad \sigma_{g_{as}} = 1.8 \text{ in/sec}$$

When the model is in the tunnel with a flutter-suppression control law engaged and subjected only to natural turbulence as excitation, control surface activity results. Analysis of data generated in the November 1989 tunnel test revealed that the RMS control surface activity predicted by simulation was much higher than actually experienced in the tunnel. Three different flutter control laws were tested in the November 1989 tunnel test and all generally resulted in the same observed RMS levels and the same degree of overprediction by the simulation. By making the turbulence intensities (σ_g) functions of dynamic pressure, simulation-predicted RMS levels can be brought into agreement with observed data. An example of this process is shown in figure 5 for the flutter suppression control law that achieved the highest dynamic pressure. The intensities required to bring batch-simulation-generated RMS results for both commanded control positions and control rates into agreement with experimental data are plotted in figure 5 as functions of dynamic pressure. For each symmetry, one intensity function corrects the RMS rate predictions and the other corrects the RMS deflection predictions. Since only one intensity exists per symmetry, either the RMS rate results or the RMS position results, but not both, can be matched. The solid lines (one per symmetry) on figure 5 represent a fitted line biased upwards. The upward bias favors overprediction, which is conservative and preferable, if small. The solid lines on figure 5 are given by the following functions,

$$\sigma_{g_{sy}} = 0.4 + 1.0\left(\frac{\bar{q}}{100}\right) \qquad \sigma_{g_{as}} = 1.6 + 2.4\left(\frac{\bar{q}}{100}\right)$$

where $\bar{q}$ has units of psf. These estimates are configuration dependent and should not be be regarded as a final characterization of turbulence in the TDT.

Aeroelastic Equations

The aeroelastic equations in a frequency domain format are given by [8,10,11]

$$\left(-\omega^2\begin{bmatrix}[M^f] & [M^{fc}]\\ [M^{cf}] & [M^c]\end{bmatrix} + j\omega\begin{bmatrix}[G^f] & 0\\ 0 & 0\end{bmatrix} + \begin{bmatrix}[K^f] & 0\\ 0 & 0\end{bmatrix}\right)\begin{Bmatrix}\eta\\ \delta\end{Bmatrix}$$

$$+ \rho\left(\frac{V}{2}\right)^2\begin{bmatrix}[Q^{ff}(j\omega)] & [Q^{fc}(j\omega)]\\ [Q^{cf}(j\omega)] & [Q^{cc}(j\omega)]\end{bmatrix}\begin{Bmatrix}\eta\\ \delta\end{Bmatrix}$$

$$= -\rho\left(\frac{V}{2}\right)^2\begin{Bmatrix}Q^{fg}(j\omega)\\ Q^{cg}(j\omega)\end{Bmatrix}\left(\frac{\xi_g}{V}\right) \qquad (1)$$

These equations consist of the standard in-vacuo second-order matrix structural equations (mass, damping, and stiffness) and apply to either symmetric or anti-symmetric motion. The flexible modes are augmented with control modes that represent control surface deflection. The control modes have zero stiffness. A low frequency subset of the elastic modes of free vibration from a large-order structural model are typically used in an aeroelastic formulation. For the AFW simulations, the number of retained flexible modes per symmetry was always between 7 and 10, inclusive. The flexible modes are orthogonal to each other so the mass and stiffness matrices are diagonal. Modal damping of 0.03 is assumed for each mode.

The in-vacuo equations were augmented with generalized aerodynamic force coefficient matrices, [Q(jω)], that are functions of frequency. The functions, [Q(jω)], can be approximated[10,11] by matrix expressions that are rational in the Laplace variable, s. The "least square"[10,11] form of approximation is given by

$$[\hat{Q}(s)] = [A_0] + [A_1]\tau s + [A_2](\tau s)^2 + \sum_{m=1}^{n_{lag}}[A_{2+m}]\left(\frac{\tau s}{\tau s+\beta_m}\right) \qquad (2)$$

where $\tau = (\bar{c}/2V)$ and n_{lag} is 1,2,3 or 4, depending on the order of the fit. Equations (1) and (2) can be combined to produce the time domain aeroelastic equations (3) in table 1, wherein the second-order, in-vacuo equations were augmented with unsteady aerodynamic "lag" states arising from the denominator term being summed in equation (2). Control surface positions, rates, and accelerations along with turbulence are treated as external inputs. The vectors $\{\eta\}$ and $\left\{x^f_{a_m}\right\}$ are both n_fx1, where n_f is the number of retained elastic modes. Equations (3) are used to solve for the elastic mode accelerations, $\{\ddot{\eta}\}$, which can be integrated to find the rates and displacements. Equations (4) in table 1 are used to calculate actuator hinge moments. A positive hinge moment in this case resists positive actuator motion. The derivative calculations indicated in equations (3) and (4) were performed for each symmetry in the simulations. The symmetric and anti-symmetric components of the final accelerometer outputs were resolved into right and left components before output.

Anti-Aliasing Filters

For all the simulations, the dynamics of the anti-aliasing filters on the 40 primary outputs were simulated. For the tunnel test, both single-pole filters with a break frequency of 25 Hz and fourth-order Butterworth filters with break frequencies of 100 Hz, had been assembled and were available. Only the single-pole filters were used in the November 1989 tunnel test. The single pole anti-aliasing filters are given by,

$$\frac{x(s)}{u(s)} = \frac{1}{(s/\omega_{aa})+1}$$

where ω_{aa} is the break frequency in radians/second.

Table 1 Aeroelastic and Hinge Moment Equations

$$\left([M^f_{\cdot}]+\rho(\frac{\bar{c}^2}{8})[A_2^{ff}]\right)\{\ddot{\eta}\} + \left([G^f_{\cdot}]+\rho(\frac{\bar{c}V}{4})[A_1^{ff}]\right)\{\dot{\eta}\} + \left([K^f_{\cdot}]+\rho(\frac{V^2}{2})[A_0^{ff}]\right)\{\eta\} - \rho(\frac{\bar{c}V}{4})\left(\left\{x^f_{a_1}\right\}+\ldots+\left\{x^f_{a_4}\right\}\right)$$

$$= -\rho(\frac{\bar{c}V}{4})\left\{A_1^{fg}\right\}\left(\frac{\dot{\xi}_g}{V}\right) - \rho(\frac{V^2}{2})\left\{A_0^{fg}\right\}\left(\frac{\xi_g}{V}\right)$$

$$-\left([M^{fc}]+\rho(\frac{\bar{c}^2}{8})[A_2^{fc}]\right)\{\ddot{\delta}\} - \left(\rho(\frac{\bar{c}V}{4})[A_1^{fc}]\right)\{\dot{\delta}\} - \left(\rho(\frac{V^2}{2})[A_1^{fc}]\right)\{\delta\} \tag{3}$$

$$\left\{\dot{x}^f_{a_m}\right\} + \beta_m\left(\frac{2V}{\bar{c}}\right)\left\{x^f_{a_m}\right\} + \left([A^{ff}_{m+2}] \quad [A^{fc}_{m+2}]\right)\begin{Bmatrix}\dot{\eta}\\ \dot{\delta}\end{Bmatrix} = -\left\{A^{fg}_{m+2}\right\}\left(\frac{\dot{\xi}_g}{V}\right) \quad (m=1,4)$$

$$\{HM_\delta\} = \begin{bmatrix}[M^{cf}]+\rho(\frac{\bar{c}^2}{8})[A_2^{cf}] & \rho(\frac{\bar{c}^2}{8})[A_2^{cc}]\end{bmatrix}\begin{Bmatrix}\ddot{\eta}\\ \ddot{\delta}\end{Bmatrix} + \begin{bmatrix}\rho(\frac{\bar{c}V}{4})[A_1^{cf}] & \rho(\frac{\bar{c}V}{4})[A_1^{cc}]\end{bmatrix}\begin{Bmatrix}\dot{\eta}\\ \dot{\delta}\end{Bmatrix}$$

$$+\begin{bmatrix}\rho(\frac{V^2}{2})[A_0^{cf}] & \rho(\frac{V^2}{2})[A_0^{cc}]\end{bmatrix}\begin{Bmatrix}\eta\\ \delta\end{Bmatrix} - \rho(\frac{\bar{c}V}{4})\left(\left\{x^c_{a_1}\right\}+\ldots+\left\{x^c_{a_4}\right\}\right) + \rho(\frac{\bar{c}V}{4})[A_1^{cg}]b(\frac{\dot{\xi}_g}{V}) + \rho(\frac{V^2}{2})[A_0^{cg}]\left(\frac{\xi_g}{V}\right) \tag{4}$$

$$\left\{\dot{x}^c_{a_m}\right\} + \beta_m\left(\frac{2V}{\bar{c}}\right)\left\{x^c_{a_m}\right\} + \left([A^{cf}_{m+2}] \quad [A^{cc}_{m+2}]\right)\begin{Bmatrix}\dot{\eta}\\ \dot{\delta}\end{Bmatrix} = -\left\{A^{cg}_{m+2}\right\}\left(\frac{\dot{\xi}_g}{V}\right) \quad (m=1,4)$$

Pre-Test and Post-Test Models

When the initial batch simulation was being developed, it was assumed the test would be conducted in Freon in the 0.8 to 0.9 Mach range, and a real possibility existed of holding Mach constant during a test run and bleeding in Freon to raise the density of the test medium. It was also expected that some of the control laws would be scheduled on dynamic pressure in which case both the batch and hot-bench simulations would need to be able to vary dynamic pressure during a run to effectively test the control laws. The aerodynamic data arrays in the simulation are strong functions of Mach in the 0.8 to 0.9 range. To interpolate each element of the aerodynamic data arrays according to Mach would require excessive CPU time. Therefore, the approach used in the both the pre-test batch and hot-bench simulations was to leave Mach and airspeed fixed and to vary the density to achieve a change in dynamic pressure.

Table 2 Pre-Test and Post-Test Simulation Math Models

State Categories	Pre-test (1-lag)		Post-test (4-lag)	
Symmetric flexible mode positions and velocities	16		20	
Sym aero lag states associated w/ the flexible modes	8		40	
Sym aero lag states associated w/ the control modes	4		16	
Symmetric turbulence states	2		2	
Anti-sym flexible mode positions and velocities	14		20	
Anti-sym aero lag states associated w/ the flexible modes	7		40	
Anti-sym aero lag states associated w/ the control modes	4		16	
Anti-sym turbulence states	2		2	
Total aeroelastic states		**57**		**156**
Actuator states, 3 per actuator, 8 actuators	24		24	
Anti-aliasing filters on 40 channels	40		40	
Total states		**121**		**220**

Some months prior to the 1989 tunnel entry, the use of Freon as a test medium was forbidden, and it was determined that the test would be conducted with air as the test medium in the 0.2 to 0.5 Mach range. In this Mach range the aerodynamic matrices are virtually constant with respect to Mach. Furthermore, in the actual wind-tunnel test, the tunnel was not evacuated to any degree. Dynamic pressure, Mach, and airspeed were all changing as the fan speed was gradually increased. In the post-test implementation, density was left fixed, while airspeed was varied to replicate a given TDT dynamic pressure.

As seen in table 2, the number of states in the post-test simulation math model is almost twice the number required in the pre-test math model. The post-test model uses 20 elastic modes instead of 15. For the post-test model, a 4-lag least-square aerodynamic fit is employed (n_{lag}=4) instead of the 1-lag fit used in the pre-test model. As seen in equations (3) and (4) and table 2, the choice of n_{lag} has a dramatic impact on the number of states.

Batch Simulation Implementation

The structure of the batch simulation is identical to the simulation math model as described by differential equations. The state derivatives are all calculated explicitly from the states (outputs of integrators). The state derivatives are collected in a vector and integrated with a Runge-Kutta second-order predictor-corrector method. The integration step used in the batch simulation is 1/2000 seconds. As indicated in figure 6, an integration step of 1/1600 seconds results in a small change in predicted response with significant degradation occurring for larger steps. In addition to the actuator, turbulence, aeroelastic, and filter dynamics, the batch simulation also simulates the digital controller. The effects of computational delay and quantization are modeled.

Pre-Test Hot-Bench Implementation

The pre-test hot-bench simulation was implemented in a manner very similar to the batch simulation. State vectors (and associated state derivative vectors) that included all but the anti-aliasing filter states were formed. The vector of state derivatives was integrated numerically with no assumptions of linearity. Once current-time flexible mode accelerations were calculated from the current-time positions and velocities, an Adams-Bashforth second-order (AB2) predictor method was used to predict the velocities at the next time step. These predicted velocities were then used in a trapezoidal integration scheme to generate predicted flexible mode positions. To wit:

$$\dot{\eta}(t+h) = \dot{\eta}(t) + \frac{1}{2}(3\ddot{\eta}(t) - \ddot{\eta}(t-h))$$

$$\eta(t+h) = \eta(t) + \frac{1}{2}(\dot{\eta}(t+h) + \dot{\eta}(t))$$

Using this modified AB2-based method, accuracy comparable to the Runge-Kutta second-order predictor-corrector formula (RK2) used in the batch simulation was achieved with a single-pass formula. Note that the RK2 formulation requires two derivative evaluations per time step, whereas AB2 is a single-pass formula which gives up some gain accuracy for phase accuracy and is typically used in real-time applications. The integration step of 1/2000 seconds used in the pre-test hot-bench simulation was small enough that the batch and hot-bench simulation results compared favorably.

The anti-aliasing filters were handled separately from the aeroelastic and actuator states. A scalar form of the state transition equations for a constant input over the interval was used. For the single-pole anti-aliasing filters given by,

$$\frac{x(s)}{u(s)} = \frac{1}{(s/\omega_{aa})+1}$$

the constant input state transition equation is

$$x(t+h) = e^{-(\omega_{aa}h)}x(t) + (1-e^{-(\omega_{aa}h)})u(t)$$

As seen in equations (3), calculating the accelerations of the elastic modes requires solving a matrix equation involving the mass matrix. If the mass matrix is constant, an inversion can be performed prior to a run (in a "reset" mode) and the

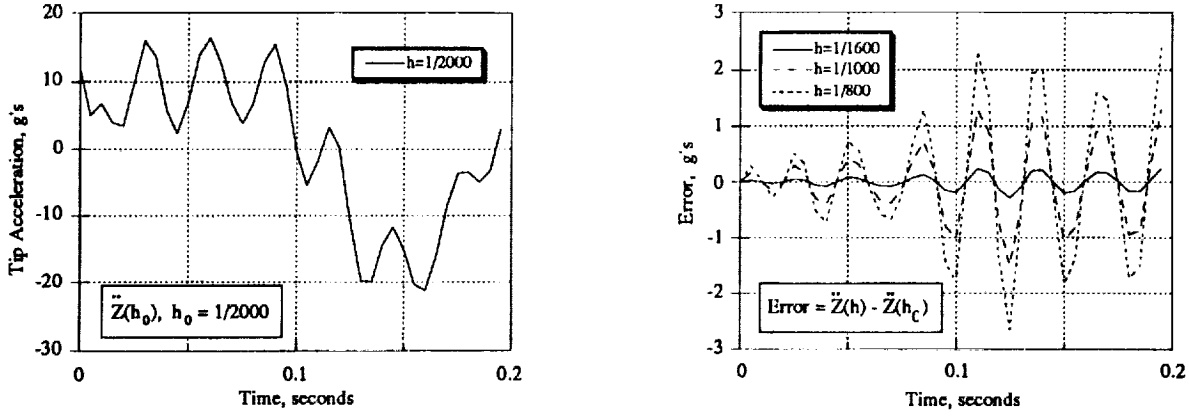

Figure 6.- Effect of step sizes on batch simulation response.

results simply stored for use as the integration proceeds. The mass matrix for the flexible modes, $[M^f_\cdot]$, (see equation (1)) is both constant and diagonal, and its inversion is trivial. The s-plane formulation used for the unsteady aerodynamic states, however, augments the mass matrix with a fully populated matrix, $[A_2^{ff}]$, that is a function of Mach number. The total mass matrix becomes

$$[M] = [M^f_\cdot] + \rho\left(\frac{\bar{c}^2}{8}\right)[A_2^{ff}]$$

$$= \left([I] + \rho\left(\frac{\bar{c}^2}{8}\right)[A_2^{ff}][M^f_\cdot]^{-1} \right)[M^f_\cdot] \qquad (5)$$

$$= \left([I] + [\Delta]\right)[M^f_\cdot]$$

If the density of the test medium, ρ, is to be varied from the simulation control console without losing time synchronization, then the mass matrix equation must be solved at each derivative evaluation. Because the elements of $[\Delta]$ in equation (5) were much smaller than unity, the following approximation was successfully used for the inverse of the mass matrix,

$$[M]^{-1} \cong [M^f_\cdot]^{-1}\left([I] - \rho\left(\frac{\bar{c}^2}{8}\right)[A_2^{ff}][M^f_\cdot]^{-1}\right)$$

When checked against the exact answer for maximum anticipated values for ρ, induced errors for the pre-test model were less than the precision available in the analog/digital converters used in the simulation loop.

Prior to the November 1989 test, an integration step size of 1/2000 seconds and a compute frame of 1/80 seconds were required for the hot-bench simulation. A compute frame of 1/80 seconds was achieved only if the AFW simulation was the only job on a Cyber 175. Thus, at best, the hot-bench simulation ran 25 (2000/80) times slower than real time, i.e., at a time scale of 1:25. A 1:25 time scale, however, proved to be burdensome while testing the controller performance evaluation mode. Sine sweeps taking 20 seconds in the tunnel would take over 8 minutes in the hot-bench lab. Modifications to the hot-bench simulation implementation, discussed in the next section, allowed the simulation to use a 1/400 second integration step, allowing a 5-fold improvement in time scale.

Post-Test Hot-Bench Implementation

The post-test hot-bench simulation implementation was driven by the need to reduce the time-scale factor to something closer to real time together with the need to accommodate the larger post-test models. If the hot-bench simulation is restricted to a fixed tunnel operating point for a given run, i.e., density, Mach, and airspeed are held fixed, then once the rate limiting is performed on the actuator transfer functions, the remaining dynamics in the simulation are linear. By utilizing a state transition method of discretization on these dynamics, the hot-bench integration step has been increased by a factor of 5, from 1/2000 to 1/400 seconds.

The post-test implementation method, wherein the hot-bench simulation is updated by data extracted from the batch simulation, is depicted schematically in figure 7. The second-order part of the third-order actuator models can be lumped with the remaining linear dynamics. The box in figure 7, labeled "Aeroelastic, Hinge Moment, and Load Equations," represents the state equations of table 1 together with algebraic output equations to estimate the required accelerometer outputs, strain gage outputs, and pressure transducer outputs from the states. Together with the 16 states associated with the second-order part of 8 actuator transfer functions and N (57 pre-test, 156 post-test) states from the aeroelastic model, a coupled linear system of N+16 states, 10 inputs (8 actuator and 2 noise), and 40 outputs can be extracted from the "linear" portion of the batch simulation. To implement the pre-test math model using the post-test state transition method required no model reduction on the extracted model, i.e., the simulation calculations could be completed in the same 1/80 second real-time clock frame used by the pre-test simulation, resulting in a time scale of 1:5. To maintain a 1:5 time scale ratio while implementing the large post-test math model will require model reduction techniques to be applied to the extracted model. Reduction methods utilizing internal balancing techniques are being investigated. Once the model has been reduced, the state transition model based on an integration step of 1/400 seconds is calculated.

The nonlinear portion involves only eight states, one from each actuator. Each state is integrated numerically with an integration step of 1/1600 seconds. Four integration steps are made to predict the value of the input to the coupled linear system at time (k+1)h where h = 1/400 seconds. Since input to the coupled linear system at time (k+1)h is now available, a trapezoidal state transition scheme can be employed. Let $\{u_k\}$ denote the quantity $\{u(kh)\}$. Given the linear dynamic system

$$\{\dot{x}\} = [A]\{x\} + [B]\{u\}$$

if the ramp input signal,

$$\{u(t)\} = \{u_k\} + (t-kh)\frac{\{u_{k+1}\} - \{u_k\}}{h}$$

is defined over the interval

$$kh \le t < (k+1)h$$

then the following exact solution for $\{x\}$ at time $t = (k+1)h$ exists

$$\{x_{k+1}\} = [F]\{x_k\} + [G_0]\{u_k\} + [G_1]\{u_{k+1}\}$$

where,

$$[F] = e^{[A]h}$$

$$[G_0] = \left(e^{[A]h}[Ah]^{-1} - [Ah]^{-1} - e^{[A]h}\right)[-A]^{-1}[B] \qquad (6)$$

$$[G_1] = \left([I] - e^{[A]h}[Ah]^{-1} + [Ah]^{-1}\right)[-A]^{-1}[B] \qquad (7)$$

Note that

$$[G] = [G_0] + [G_1] = \left([I] - e^{[A]h}\right)[-A]^{-1}[B]$$

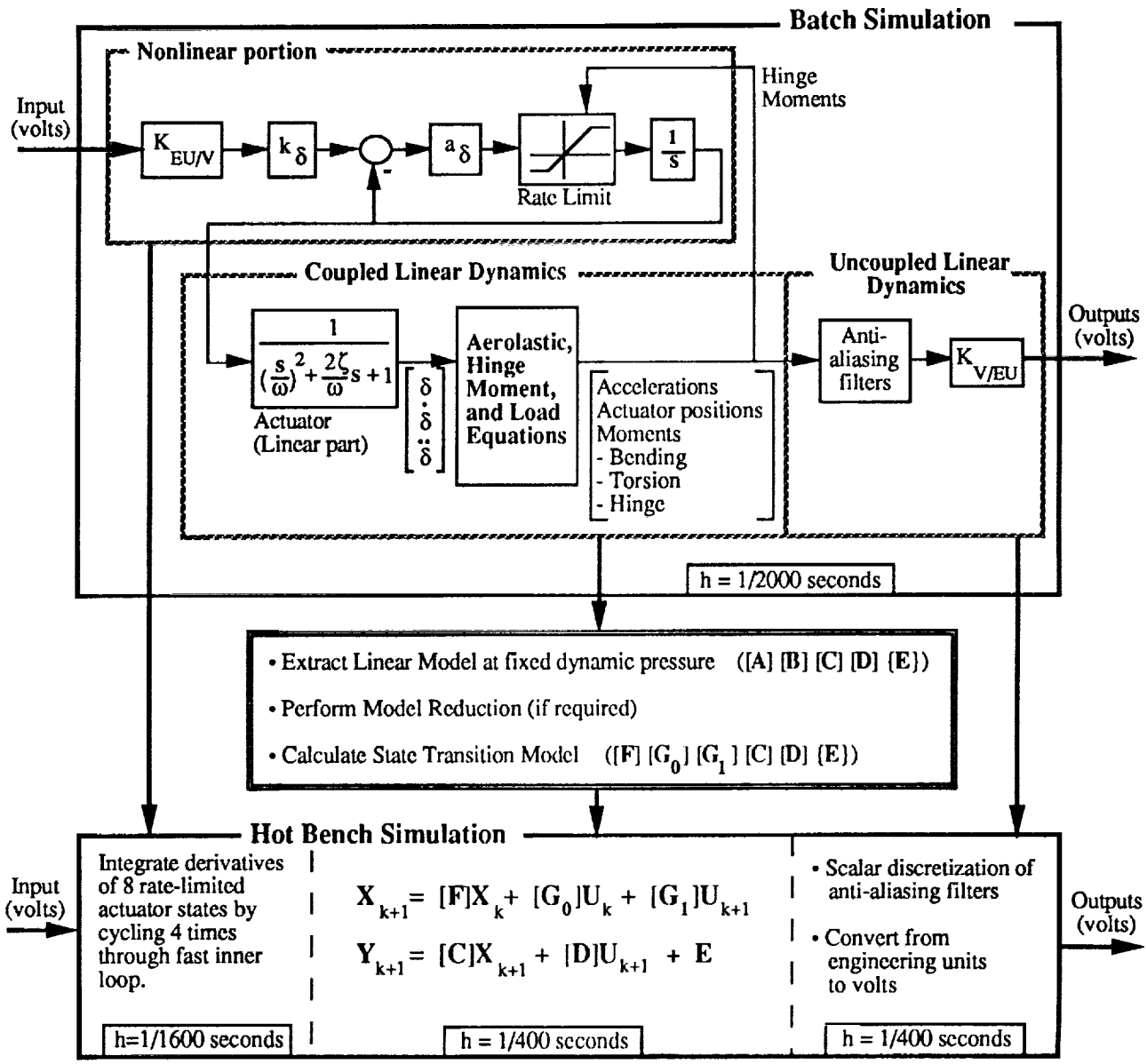

Figure 7.- Data flow from the batch to the hot-bench simulation.

which corresponds to the result one expects to see for [G] if u(t) is assumed to be constant over the interval

$$kh \le t < (k+1)h$$

Clearly, the direct evaluation of $[G_0]$ and $[G_1]$ using equations (6) and (7) will not work if [A] is singular, as would occur if [A] included rigid body modes with zero eigenvalues. However, using the Taylor series expansion

$$e^{[A]h} = [I] + [A]h + \frac{1}{2}([A]h)^2 + \ldots$$

$$= \sum_{p=0}^{\infty} \frac{1}{p!}([A]h)^p$$

and recognizing that

$$([A]h)e^{[A]h} = e^{[A]h}[A]h$$

the equations for $[G_0]$ and $[G_1]$ can be put into a form that can be calculated if [A] has zero eigenvalues. Thus,

$$[G_0] = \left(\sum_{p=2}^{\infty} \frac{1}{p!}(-1)^p ([A]h)^{p-2} \right) h\, e^{[A]h}\, [B]$$

$$[G_1] = \left(\sum_{p=2}^{\infty} \frac{1}{p!}([A]h)^{p-2} \right) h\, [B] \qquad (8)$$

The matrices $[G_0]$ and $[G_1]$ can be calculated by summing the above series until the next term is under some tolerance. When applied to the pre-test model, procedures to sum the series defined by equations (8) converged without difficulty.

The anti-aliasing filters are applied individually to each output signal, which results in a diagonal system. The anti-aliasing filters are therefore not lumped with the coupled linear system to avoid making full matrix operations. The anti-aliasing filter dynamics are digitized in a sequential manner utilizing a scalar form of the trapezoidal state transition method described above. For single pole anti-aliasing filters given by

$$\frac{x(s)}{u(s)} = \frac{1}{(s/\omega_{aa})+1}$$

the state transition equations are

$$x(t+h) = e^{-(\omega_{aa}h)}x(t) + g_0u(t) + g_1u(t+h)$$

where

$$g_0 = -e^{-(\omega_{aa}h)}(\omega_{aa}h)^{-1} + (\omega_{aa}h)^{-1} - e^{-(\omega_{aa}h)} \quad (9)$$

$$g_1 = 1 + e^{-(\omega_{aa}h)}(\omega_{aa}h)^{-1} - (\omega_{aa}h)^{-1} \quad (10)$$

Note that the term $\left(-[A]^{-1}[B]\right)$ in (6) and (7) becomes unity in equations (9) and (10).

Verification

The hot-bench simulation was verified by comparing time history results with the batch simulation. Trajectories were found to match within the width of plotted lines. The open-loop plant dynamics of the batch simulation were verified by comparison with ISAC-generated linear models. For each symmetry, a linear model was extracted from the batch simulation using finite differencing. A batch-generated symmetric model and an ISAC-generated symmetric model had different numbers of states because of the way the actuators were handled. The batch-derived model had dynamics for eight right and left control surfaces and the ISAC model had dynamics for only four symmetric control deflections. The corresponding batch and ISAC linear models were compared by overlaying the gain and phase frequency response of each input/output pair. The agreement between ISAC-generated and batch-simulation-derived frequency responses was excellent.

Concluding Remarks

Two simulations, one batch and one real-time, of an aeroelastically scaled wind-tunnel model were described. The batch simulation was used to generate and verify the real-time simulation and to test candidate control laws prior to implementation on the control computer. The real-time simulation supported hot-bench testing of a digital controller developed to actively control the elastic deformation of the wind tunnel model. Time scaling required for hot-bench testing was discussed. Substantial improvement in the time scale ratio was achieved by application of state transition methods.

References

1. Noll, T.; et al.: *Aeroservoelastic Wind-Tunnel Investigations Using the Active Flexible Wing Model - Status and Recent Accomplishments.* NASA TM-101570 and AIAA Paper 89-1168. Presented at the AIAA/ASME/ASCE/AHS 30th Structures, Structural Dynamics, and Materials (SDM) Conference in Mobile, Alabama, April 1989.

2. Perry, B.; Mukhopadhyay, V.; Hoadley, S.; Cole, S.; Buttrill, C.; and Houck, J.: *Digital-Flutter-Suppression-System Investigations for the Active Flexible Wing Wind-Tunnel Model.* NASA TM-102618 and AIAA Paper 90-1074. Presented at the AIAA/ASME/ASCE/-AHS 31st Structures, Structural Dynamics, and Materials (SDM) Conference in Long Beach, CA, April 1990.

3. Cole, S.; Perry, B.; and Miller, G: *An Overview of the Active Flexible Wing Program.* Presented at the Fourth Workshop on Computational Control of Flexible Aerospace Systems, Williamsburg, VA, July 11-13, 1990.

4. Miller, G: *Active Flexible Wing (AFW) Technology.* NA-87-1515L, 1987.

5. Crawford, D.; Cleveland, J.; and Staib, R.: *The Langley Advanced Real-Time Simulation (ARTS) System Status Report.* AIAA-88-4595-CP, September 1988.

6. Hoadley, S.; Buttrill, C.; McGraw, S. and Houck, J.: *Development, Simulation Validation, and Wind-Tunnel Testing of a Digital Controller System for Flutter Suppression.* Presented at the Fourth Workshop on Computational Control of Flexible Aerospace Systems, Williamsburg, VA, July 11-13, 1990.

7. Pototzky, T.; Wieseman, C.; Hoadley, S. and Mukhopadhyay, V.: *Development and Testing of Methodology for Evaluating the Performance of Multi-Input/Multi-Output Digital Control Systems.* AIAA Paper 90-3501. Presented at the AIAA Guidance, Navigation, and Control Conference in Portland, Oregon, August 20-22, 1990.

8. Peele, E. and Adams, W.: *A Digital Program for Calculating the Interaction Between Flexible Structures, Unsteady Aerodynamics, and Active Controls.* NASA TM-80040, January 1979.

9. Hoblit, F.: *Gust Loads on Aircraft: Concepts and Applications,* AIAA Education Series, American Institute of Aeronautics and Astronautics, Inc., Washington, DC, 1988.

10. Tiffany, S.; and Adams,W.: *Nonlinear Programming Extensions to Rational Function Approximation Methods for Unsteady Aerodynamic Forces Which Allow Variable Selection of Constraints,* NASA TP-2776, May 1988.

11. Tiffany, S.; and Karpel, M.: *Aeroservoelastic Modeling and Applications Using Minimum-State Approximations of the Unsteady Aerodynamics.* NASA TM-101574 and AIAA Paper 89-1188. Presented at the AIAA/ASME/-ASCE/AHS 30th Structures, Structural Dynamics, and Materials (SDM) Conference in Mobile, AL, April 1989.

Appendix A - Input/Ouput List for AFW Wind-Tunnel Model and Simulations

Table A.1 Simulation and Wind-Tunnel Model Inputs and Scaling

No.	Signal	Volts/Unit	Units
1	Left LEO actuator command, + leading edge down	0.375	degrees streamwise
2	Left LEI actuator command, + leading edge down	0.375	degrees streamwise
3	Right LEI actuator command, + leading edge down	0.375	degrees streamwise
4	Right LEO actuator command, + leading edge down	0.375	degrees streamwise
5	Left TEO actuator command, + trailing edge down	0.375	degrees streamwise
6	Left TEI actuator command, + trailing edge down	0.375	degrees streamwise
7	Right TEI actuator command, + trailing edge down	0.375	degrees streamwise
8	Right TEO actuator command, + trailing edge down	0.375	degrees streamwise

Table A.2 Simulation and Wind-Tunnel Model Outputs and Scaling

No.	Signal	Volts/Unit	Units
1	Left LEO actuator position, RVDT, + leading edge down	0.375	degrees streamwise
2	Left LEI actuator position, RVDT, + leading edge down	0.375	degrees streamwise
3	Right LEI actuator position, RVDT, + leading edge down	0.375	degrees streamwise
4	Right LEO actuator position, RVDT, + leading edge down	0.375	degrees streamwise
5	Left TEO actuator position, RVDT, + trailing edge down	0.375	degrees streamwise
6	Left TEI actuator position, RVDT, + trailing edge down	0.375	degrees streamwise
7	Right TEI actuator position, RVDT, + trailing edge down	0.375	degrees streamwise
8	Right TEO actuator position, RVDT, + trailing edge down	0.375	degrees streamwise
9	Model pitch actuator position, RVDT, + nose up	0.375	degrees
10	Model roll position, + right wing down	0.0555	degrees
11	Left LEO co-located accelerometer, + up	0.5	g
12	Right LEO co-located accelerometer, + up	0.5	g
13	Left TEO co-located accelerometer, + up	0.5	g
14	Left TEI co-located accelerometer, + up	0.5	g
15	Right TEI co-located accelerometer, + up	0.5	g
16	Right TEO co-located accelerometer, + up	0.5	g
17	Left wingtip accelerometer, + up	0.5	g
18	Right wingtip accelerometer, + up	0.5	g
19	Left store-mounted accelerometer, + up	0.5	g
20	Right store-mounted accelerometer, + up	0.5	g
21	Fuselage accelerometer # 1, + up	1.0	g
22	Fuselage accelerometer # 2, + up	1.0	g
23	Fuselage accelerometer # 3, + up	1.0	g
24	Roll rate, + right wing down	0.0224	deg/sec
25	Left outboard bending moment, + tip up	0.00244	in-lb
26	Left inboard bending moment, + tip up	0.000477	in-lb
27	Right inboard bending moment, + tip up	0.000553	in-lb
28	Right outboard bending moment, + tip up	0.002820	in-lb
29	Left outboard torsion moment, + leading edge up	0.00611	in-lb
30	Left inboard torsion moment, + leading edge up	0.000112	in-lb
31	Right inboard torsion moment, + leading edge up	0.000106	in-lb
32	Right outboard torsion moment, + leading edge up	0.00702	in-lb
33	Left LEO actuator hinge moment, + leading edge up	0.014760	in-lb
34	Left LEI actuator hinge moment, + leading edge up	0.014144	in-lb
35	Right LEI actuator hinge moment, + leading edge up	0.014155	in-lb
36	Right LEO actuator hinge moment, + leading edge up	0.020503	in-lb
37	Left TEO actuator hinge moment, + trailing edge up	0.026917	in-lb
38	Left TEI actuator hinge moment, + trailing edge up	0.014592	in-lb
39	Right TEI actuator hinge moment, + trailing edge up	0.013616	in-lb
40	Right TEO actuator hinge moment, + trailing edge up	0.028341	in-lb
41	Wind Tunnel Mach number	10.0	Mach number
42	Wind Tunnel Dynamic Pressure	.006945	PSI

NASA
National Aeronautics and Space Administration

Report Documentation Page

1. Report No.	2. Government Accession No.	3. Recipient's Catalog No.
NASA TM-102758		

4. Title and Subtitle
Hot-Bench Simulation of the Active Flexible Wing Wind-Tunnel Model

5. Report Date
November 1990

6. Performing Organization Code

7. Author(s)
Carey S. Buttrill
Jacob A. Houck

8. Performing Organization Report No.

10. Work Unit No.
505-64-20-01

9. Performing Organization Name and Address
NASA Langley Research Center
Hampton, VA 23665-5225

11. Contract or Grant No.

13. Type of Report and Period Covered
Technical Memorandum

12. Sponsoring Agency Name and Address
National Aeronautics and Space Administration
Washington, DC 20546-0001

14. Sponsoring Agency Code

15. Supplementary Notes
Presented as AIAA Paper No. 90-3121 at the AIAA Flight Simulation Technologies Conference, September 17-19, 1990, Dayton, Ohio.

16. Abstract

Two simulations, one batch and one real-time, of an aeroelastically scaled wind-tunnel model were developed. The wind-tunnel model was a full-span, free-to-roll model of an advanced fighter concept. The batch simulation was used to generate and verify the real-time simulation and to test candidate control laws prior to implementation. The real-time simulation supported hot-bench testing of a digital controller, which was developed to actively control the elastic deformation of the wind-tunnel model. Time scaling was required for hot-bench testing. The wind-tunnel model, the math models for the simulations, the techniques employed to reduce the hot-bench time-scale factor, and the verification procedures are described.

17. Key Words (Suggested by Author(s))	18. Distribution Statement
Flexible, Simulation, Aircraft, Real-time	Unclassified - Unlimited Subject Category 08

19. Security Classif. (of this report)	20. Security Classif. (of this page)	21. No. of pages	22. Price
Unclassified	Unclassified	13	A03